A Comparison of Brightness Temperatures Derived from Geostationary and Polar Orbiting Satellites.
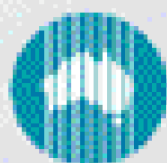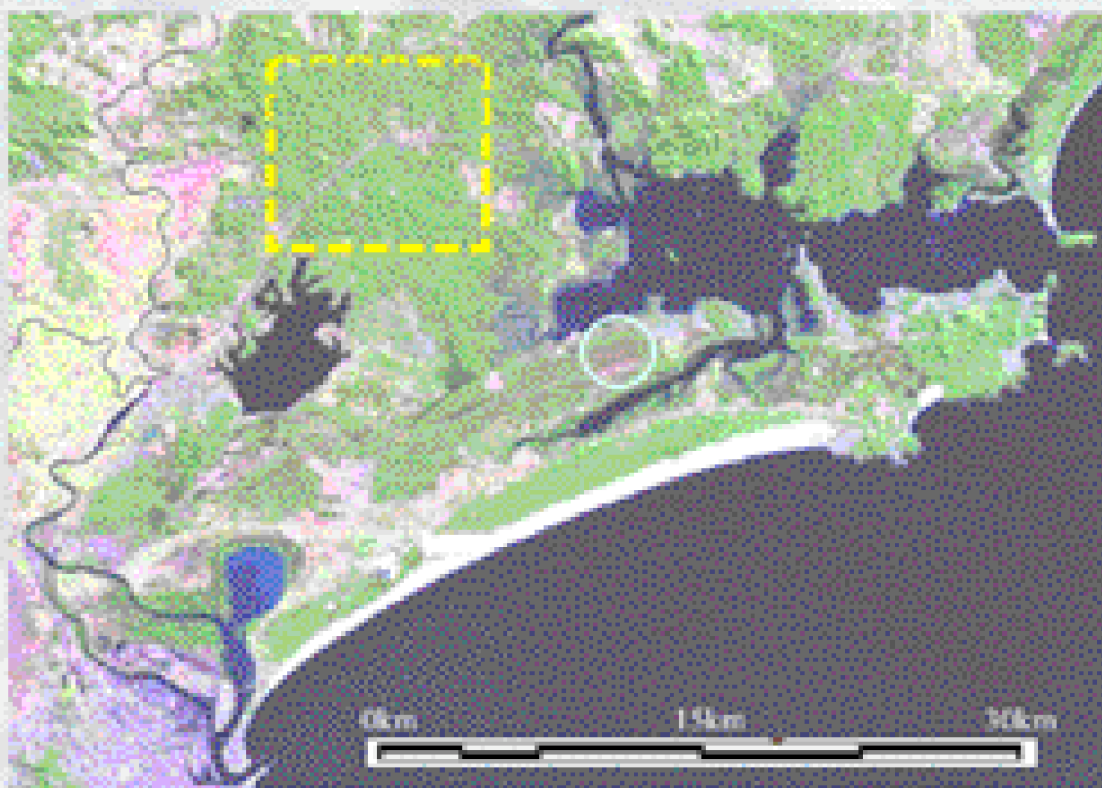
M. F. McCabe, A. J. Prata and J. D. Kalma

A Comparison of Brightness Temperatures Derived from Geostationary and Polar Orbiting Satellites.

M. F. McCabe[*], A. J. Prata[#] and J. D. Kalma[*]

[*] School of Engineering, University of Newcastle, Callaghan, NSW 2308, Australia.
[#] CSIRO Atmospheric Research, Private Bag 1, Aspendale, VIC 3195, Australia.

Abstract

In this report we examine the feasibility of extracting a temporal sequence of brightness temperatures (BT) derived from the Japanese Space Agency's Geostationary Meteorological Satellite (GMS) using the on board visible and infrared spin-scan radiometer (VISSR). This particular platform offers the potential to extract brightness temperatures at approximately hourly intervals, providing a means to monitor the diurnal trend in land surface temperature (LST). This can be achieved using a number of techniques including the commonly used split-window approaches. While the focus of this report is directed at brightness temperatures, the findings have direct implications for the derivation of LST. Additional information has been obtained using data from the National Oceanic and Atmospheric Administration's (NOAA) Advanced Very High Resolution Radiometer (AVHRR) instrument on board the NOAA-12 and NOAA-14 satellites. This instrument provides a more detailed spatial resolution with a corresponding decrease in temporal resolution in the order of four images per day.

Information related to the extraction of brightness temperatures from each of these platforms, along with a detailed inter-comparison between the two is presented. The effects of heterogeneity at the land surface is also examined through spatial averaging of NOAA brightness temperatures and their comparison with colocated GMS values. Particular attention is directed towards the effects of angular variation and other sources of disparity between the brightness temperature predictions of the two remote sensors. It is expected that an analysis of concurrent NOAA and GMS brightness temperatures may yield insight into the production of spatially or temporally enhanced predictions of the LST which would prove useful in a variety of modelling applications.

1.   Introduction

Remotely sensed measurements of the earth's surface have the potential to provide detailed information on land surface properties and parameters. One of the major advantages of satellites is their ability to obtain information at a regional scale as opposed to the point scale estimation of conventional ground based data collection techniques. This feature provides an ideal platform from which to monitor regional land surface processes. Thermal infrared measurement of the land surface has the potential to supply relatively accurate measures of brightness temperatures (BT) from which the land surface temperature (LST) can be predicted at a range of spatial and temporal scales. Remote sensing offers a viable method for determining these patterns at various scales, and much research has been directed into improving predictions from these sources (Prata, 1994; Becker and Li, 1995; Jackson, 1997).

The determination of temperature from remote sensors can also provide a valuable data source with which to initialise and calibrate a variety of modeling applications. Recent advances in data assimilation aimed at refining model predictions, also make the use of these remote estimates of the land surface attractive. Remotely sensed temperatures from both the land and sea have been used in a number of applications including monitoring of carbon dioxide (CO_2) emission from the ocean (Boutin *et al.*, 1999), estimation of the surface radiation budget (Nunez and Kalma, 1996), modeling of regional scale evapotranspiration (McCabe *et al.*, 2001) and surface fluxes (Diak and Stewart, 1989; Kustas and Humes, 1996) and also moisture availability (McVicar and Jupp, 1998). Improvements in the understanding and accuracy of brightness temperature measurements will lead to improved estimates of the LST and facilitate its use in a wide variety of applications.

Accurate prediction of LST however is difficult due to a number of underlying factors which provide some interesting challenges. Amongst these are issues of spatial and temporal resolution, land surface heterogeneity and atmospheric and land surface effects. The atmosphere is not a perfect emitter and absorption, primarily by water vapour and CO_2 in clear atmospheric conditions, affects the accuracy of the sensed infrared radiation. Cloud cover increases the difficulties associated with absorption effects. A further complication is the imperfect emittance of the land surface, characterised by the emissivity of an object. While this element can in theory be accounted for, surface heterogeneity complicates the task in practice. There are a number of techniques available to account for the atmospheric correction and emissivity problems identified above. One of these is the theoretically derived split-window approach (McMillin and Crosby, 1984). Accounting for obfuscatory factors allows a more accurate and hence useful prediction of LST to be derived.

This report does not explore in any depth the actual determination of the LST. The focus of this report is an inter-comparison of BT from two distinct platforms, from which LSTs can be calculated. Examination of the different spatial and temporal characteristics of these platforms may offer insight into the development of a spatially refined temperature product. Future investigations aim to incorporate the split-window approaches to determine broad scale surface responses and compare these with in-situ measurements (McCabe *et al.*, 2001). This scale analysis will prove

useful in an assessment of the suitability of remote measurements in regional scale land surface modelling.

GMS-VISSR and NOAA-AVHRR Sensor Characteristics

The Geostationary Meteorological Satellite (GMS) is operated by the Japanese Meteorological Agency as part of a global system of meteorological satellites. The current operational satellite is GMS-5, launched in March of 1995. This satellite is positioned in a geostationary orbit located 35,000 km above the equator at a longitude of 140°E (GMS User's Guide, 1997) providing complete coverage of continental Australia. Full disk images from the platform are relayed to a ground based receiving station approximately 25-28 times a day. Incoming radiation is sensed by a visible and infrared spin scan radiometer (VISSR). Relevant specifications of the GMS-5 satellite are outlined in Table 1.

Table 1: Characteristics of the GMS-VISSR and NOAA-AVHRR satellites

		GMS-VISSR	NOAA-AVHRR (12&14)
Orbit		Geo-Synchronous	Polar
Quantization Level		2^8	2^{10}
Spatial	VIS	1.25km	1.1km (nadir)
Resolution	IR	5km	1.1km (nadir)
Channels	VIS-1	0.55 - 0.90µm	0.58 - 0.68µm
	VIS-2	-	0.725 - 1.10µm
	IR-1 (4[*])	10.5 - 11.5µm	10.3 - 11.3µm
	IR-2 (5[*])	11.5 - 12.5µm	11.5 - 12.5µm
	IR-3 (3[*])	6.5 - 7.0µm	3.55 - 3.93µm
Height		35,800km	850km
Repeat Rate		hourly	10 hourly
IFOV	VIS	35x31µrad	1300 µrad
	IR	140x140µrad	(0.0745 degrees)

• Refers to the order of channels on the NOAA-AVHRR

The National Oceanic and Atmospheric Administration (NOAA) operates a series of polar orbiting satellites that circle the Earth in an almost north-south orbit, passing close to both poles. The orbits are elliptical with an altitude of between 830 km during the morning overpass and approximately 870 km in the afternoon. NOAA is currently operating two polar orbiters: NOAA-14, launched in 1994 and NOAA-16 which is one of a new series of satellites incorporating improved sensors. NOAA-12, which was launched in 1991, continues transmitting data as a standby satellite. The satellites used in this study are the NOAA-12 and NOAA-14, details of which can be found in Table 1.

The Advanced Very High Resolution Radiometer (AVHRR) sensor is on board the NOAA series of satellites. This scanning radiometer uses 5 (6 in the case of NOAA-16) detectors each of which 'senses' the intensity of different wavelengths of electromagnetic (EM) radiation. The major advantage of the polar orbiting satellites over their geostationary counterparts is the increased spatial resolution. The drawback with this orbit is the lower temporal resolution, with the two NOAA satellites

transmitting a combined total of between 4 to 6 images per day, dependant on the time of overpass and the effects of orbital decay.

Location of Study Area

The area that forms the focus of this investigation is located on the mid-north coast of New South Wales, 35 km north of Newcastle. The area under investigation is located near an important groundwater source which provides approximately a third of the total water requirements for the Hunter region. This aquifer system covers an areal extent of approximately 275 km^2. Figure 1 depicts a false colour LANDSAT scene of a section of the area under investigation. The predominate land use in this portion of the catchment is rural/agricultural. The land surface is relatively flat with forest and scrubland forming the major vegetative component, interspersed with grassland areas.
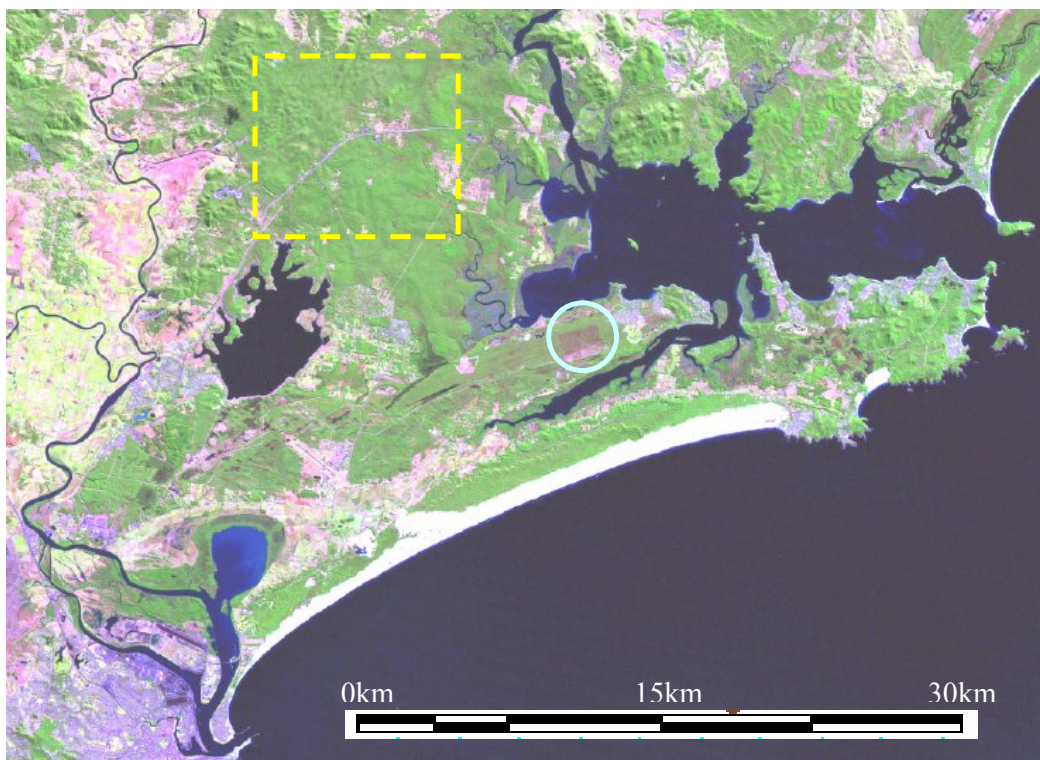
Figure 1. LANDSAT-7 image from January 2001 captured over a region north of Newcastle, NSW which encompass a series of important groundwater aquifers. The image is a false colour composite with the study area bounded by the dashed square. Newcastle is towards the bottom left hand corner of the image. A recent field investigation using multi-scale remote sensing and ground based infrared thermometry has been undertaken at a location within the groundwater area outlined with a circle.

2.   Estimation of a Brightness Temperature Sequence

Infrared remote sensing offers the potential to provide insight into the monitoring and modelling of the surface energy budget at regional and global scales. However, there are difficulties in utilising thermal observations due to unknown surface emissivities, atmospheric corrections and the presence of numerous variables affecting the relationship between thermal radiance and the partitioning of energy fluxes (Norman *et al.*, 1995). The GMS and NOAA satellites are equipped with infrared radiometers designed to measure the up-welling radiation from the earth's surface. These radiometers detect infrared EM radiation in two distinct regions referred to as atmospheric windows, namely between 3.5-3.9 μm and 10-13 μm. These regions are relatively free from atmospheric absorption, making them suitable for determining a land surface temperature. There is an additional complication at the land surface due to its characteristic departure from black body behaviour (a black body is a perfect emitter of infrared radiation). The degree to which this affects the EM radiation can be quantified in terms of its emissivity. In practice however, quantifying this variable is extremely difficult due to the high variability of natural surfaces (Prata, 1994).

Land Surface Temperature (LST)

The key land surface variable that can be derived from remotely sensed brightness temperatures is the LST. Temperature estimates of the land are integral in the quantification of energy fluxes and facilitate the prediction of evapotranspiration. Difficulties associated with the extraction of LST from remotely sensed imagery provide considerable uncertainty in subsequent predictions. There have been a number of attempts to more accurately extract temperature measurements from a variety of remote sensing platforms (Seguin *et al.*, 1994; Norman *et al.*, 1995; Prata and Cechet, 1999). Most have focused on either the NOAA-AVHRR series of satellites or geostationary platforms such as the GOES or METEOSAT. To date, relatively few studies have focused on an examination of the GMS-VISSR.

Prata and Cechet (1999) showed that LST estimates from the GMS-VISSR can be determined to RMS accuracies of 2-3K when compared with contact temperature transducers installed at a field site. They contend that accuracies of 3K are of marginal use, whereas predictions of around 1K would be of potentially great benefit in modeling applications. The use of spatial and temporal patterns of LSTs offer alternative methodologies that acknowledge and incorporate the inherent uncertainty in absolute temperature values. Temperature difference approaches retain the characteristic features of the diurnal pattern while removing the reliance on absolute accuracy (McVicar and Jupp, 1998; Norman *et al.*, 2000; McCabe *et al.*, 2001). Continued advances in increasing the accuracy of LST estimates and the development of innovative methods to incorporate remotely sensed information into a variety of modeling approaches, offer much towards the improvement of model predictions.

Two major problems in the use of infrared remote sensing to estimate LST can be classified into atmospheric and land surface effects. The methods currently used to account for these factors also fall into two broad categories. Norman *et al.* (1995)

describe techniques that combine *in-situ* measurements of surface temperature and moisture, often through atmospheric soundings, coupled with atmospheric radiative transfer models such as LOWTRAN-7 (Kneizys *et al.*, 1988) as direct methods. Alternatively, indirect methods may use atmospheric radiative transfer models with soundings of the atmosphere from instruments such as the TIROS Operational Vertical Sounder (TOVS), or they may be based on split-window algorithms using infrared channels (IRC) 4 and 5 of the NOAA-AVHRR satellite. A discussion of the split-window approach is presented in the following section.

Split-Window Techniques

Split-window equations offer one approach in determining LSTs from remotely sensed brightness temperatures by making use of the close correlation between the transmission of different wavelengths along the same path. Through the use of two infrared channels, for example those on-board the NOAA-AVHRR or GMS-VISSR, an exploitation of the differential absorption effect can be utilised. As it is often more convenient to use temperatures as opposed to radiances, an approximation is required. A first order Taylor series expansion of the Plank function about a mean temperature $\bar{T}$ is applied, which allows the generalised form of the split-window equation to be derived (Prata, 1993);

$$\mathbf{LST} = \mathbf{b_0}(\varepsilon, u, \theta)\mathbf{T}_i + \mathbf{c_0}(\varepsilon, u, \theta)\mathbf{T_j} + \mathbf{d_0}(\varepsilon, u, \theta, R) \qquad \textbf{Eq. 1}$$

where: ε = emissivity
u = total water vapour in column
θ = viewing zenith angle
R = atmospheric down-welling radiance
T_i, T_j = brightness temperature in IR Channels i and j
b_0, c_0, d_0 = surface specific coefficients

The approximations used to determine these split-window relations are generally similar, with the equations derived for: (i) flat terrain, resulting in minimal shading influences; (ii) relatively homogenous surfaces at the scale of satellite resolution; (ii) Lambertian surface; (iv) precipitable water amounts of less than $2g/cm^2$; and (v) clear-sky conditions (Prata, 1993). In practice, sufficient accuracy can still be obtained even if these restrictions are not closely met. The specification of a meaningful emissivity value however, has a large effect on the accuracy of LST predictions.

A number of theoretical algorithms similar in form to that shown above, have been developed to account for the various factors affecting accurate determination of land surface temperature (Kerr *et al.*, 1992; Becker and Li, 1995; Coll and Casselles, 1997). There has been considerable research on the dependence of satellite derived temperature estimates on the emissivity (ε) and water content (ω), but relatively little in regard to the viewing angle (θ) and atmospheric down-welling radiance (R).

Cloud Detection

The effects of cloud pose the greatest obstacle to an effective examination of the diurnal variation in brightness temperatures. Apart from inspection of the visible channel to actually 'look' for cloud cover, an alternative approach is to examine the

difference between infrared channels. For local atmospheric and meteorological conditions it was decided that a discrepancy of more than 3K would indicate pixel contamination with clouds, due to differential absorption in the infrared channels being a function of the atmospheric precipitable water content (note that in the tropics, differences of up to 5K in IR channels can occur even under cloud free conditions). This technique provides a relatively simple but efficient method of resolving cloud contamination issues. However difficulties in identifying contamination of pixels during the night time still remain.

Brightness Temperature Data

The derivation of LST from brightness temperatures using split-window algorithms, as shown above, is relatively straightforward. The accuracy of this estimate on the other hand is more contentious. To examine the relative accuracy of predicting temperatures from remote platforms, an inter-comparison of the thermal channels on board the NOAA and GMS platforms was undertaken. Examination of the NOAA-12 and 14 AVHRR and the GMS-5 VISSR sensors was undertaken for two relatively cloud free periods. The periods combine a total of 10 days, with 260 GMS and 41 coincident NOAA overpasses being examined. The images span the period 16-28 March 1997, and encompass both day and night time observations. Measurements of the calibrated brightness temperature in Channels 4 and 5 of the AVHRR and Channels 1 and 2 of the VISSR were extracted to allow platform inter-comparison (ref. Appendix A).

Values from the GMS-VISSR platform that did not coincide with the NOAA-AVHRR time of overpass by more than ten minutes were temporally averaged to produce a comparable response. For example, if the NOAA overpass occurred at 10 a.m., the GMS readings for 9:30 a.m. and 10:30 a.m. were linearly interpolated. Although this may introduce some error into the temporal patterns, this occurred only three times throughout the period of study and on all occasions corresponded to cloud free period, making the interpolation of the GMS brightness temperature reasonably accurate.

To examine the degree of heterogeneity at the land surface a number of properties were examined. Four adjacent GMS pixel locations were identified within the study region and their values extracted. Examination of these values provided some indication of the level of surface temperature variation across a large spatial extent. A series of NOAA measurements were then colocated to a single GMS response. Expanding a 5x5 area of brightness temperatures around the central NOAA value allowed direct comparison to the GMS response.

The twenty-five individual AVHRR pixels were spatially averaged and compared with the single GMS response based on an equal area approximation. Figure 2 illustrates the derived brightness temperatures from both the GMS-VISSR and NOAA-AVHRR satellites for two infrared channels. The unbroken line represents the single GMS pixel to which the NOAA observations were colocated to, while the dashed sequence illustrate the other three GMS responses. Both a 1x1 and a 5x5 averaged brightness temperature are also plotted.

In instances where the zenith angle is large, at the edge of the AVHRR swath for example, the sensed area is significantly elongated as opposed to the 1 km^2 pixel size at nadir. Although the spatial resolution and viewing geometry of the pixels across platforms are not equivalent the following justifications were put forward for the use of an equal area approximation in subsequent analysis:

i.   There is a close correlation between the sequences derived from adjacent GMS pixels. While there is some discrepancy at the diurnal peaks across the four sequences, both the diurnal rise and fall of the curve illustrate the high degree of consistency, with brightness temperature variations generally the result of intermittent cloud cover. In the few instances where the 5x5 NOAA pixels may have a larger extent than the single GMS pixel (i.e. at large NOAA zenith angles), the variation at the surface should not significantly affect resulting brightness temperatures for this reason;

ii. There is good agreement between the 5x5 and 1x1 AVHRR observations. Table 2 lists the differences between 3x3 and 5x5 spatial averages from their central pixel, with a maximum average temperature difference of 0.28K; and

iii. This was explored further with a plot of the differences between the 3x3 and 5x5 averaged NOAA brightness temperatures from the central NOAA observation, reproduced in Figure 3 below. As can be seen, there is a trend towards a decrease in brightness temperature differences for larger zenith angles, corresponding to the most geometric distortion. Overall, the differences do not generally exceed ±0.5K. Two values have been excluded from Figure 3 for presentation purposes as their differences were −1.4K and 1.85K. The zenith angles for these values were 12° and 52° respectively, the latter having the same atmospheric path length as GMS observations. These spurious values may be the result of sub-pixel cloud cover, which passed the simple cloud detection routine used here.

For strongly heterogeneous surfaces it would be more critical to average the observed radiances and derive brightness temperatures from these, as opposed to direct averaging of the brightness temperatures employed here. This issue is discussed further in Section 3.

From Figure 2 it can be observed that the magnitude of the differences in the peaks between the two infrared channels for both the GMS and NOAA brightness values is not the same. Table 2 presents these differences for NOAA 1x1 and 5x5 averages and the single GMS observation. The differences between the IR channels for the NOAA estimates are significantly more than the inter-channel difference in the GMS with an average decrease across the peak values in the NOAA of around 2.3K compared to a 1K difference in the GMS. Importantly, the difference is quite similar across the areal average.

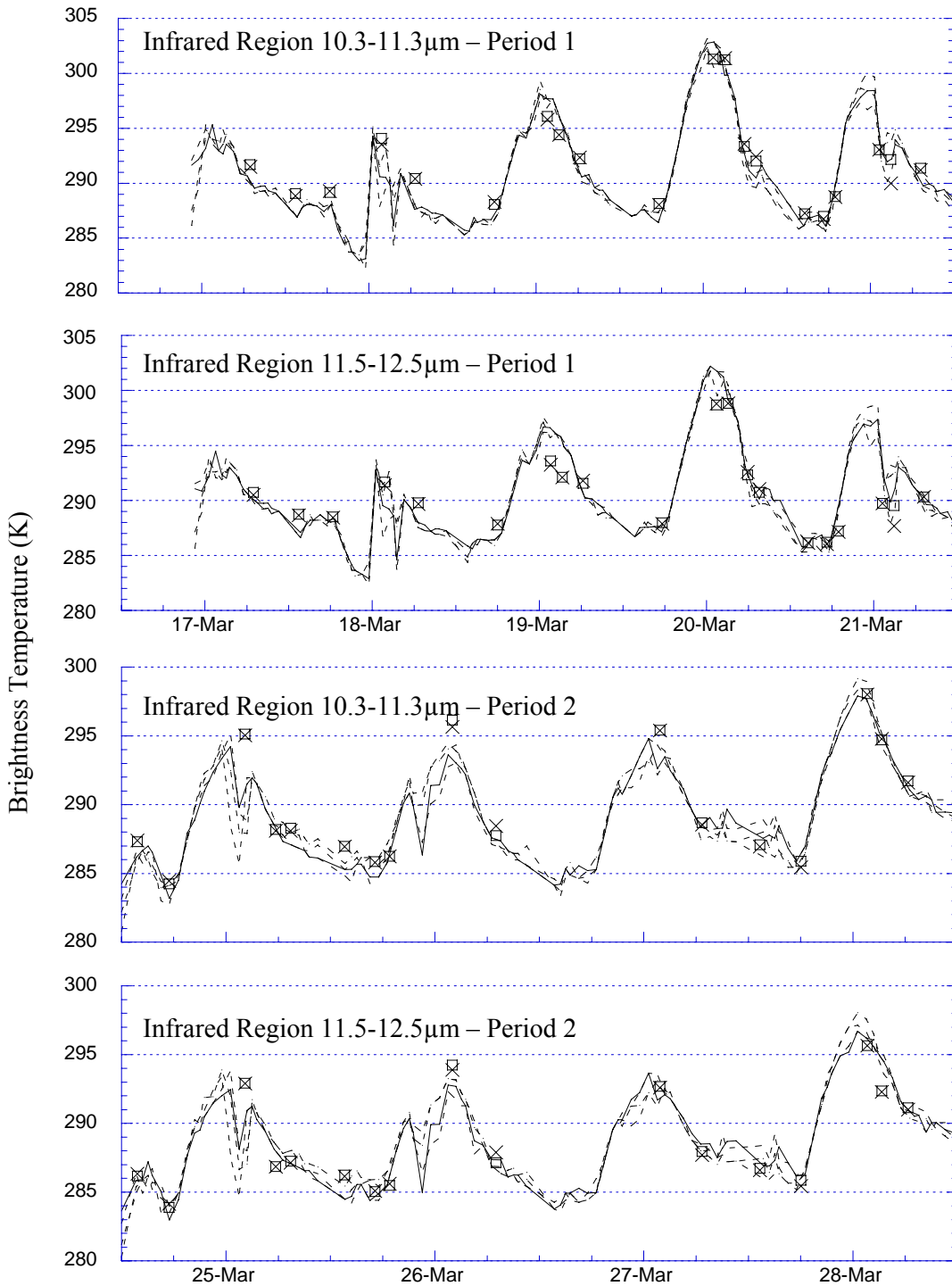**Figure 2. Evolution of infrared brightness temperature. NOAA values are represented by a 1x1 central pixel (×) and a 5x5 spatial average (□). There are four adjacent GMS signatures with the response colocated with the NOAA images represented by a solid line. Period 1 analyses data from the 17-21 March and Period 2 covers 24-28 March. Both periods start and finish at midnight, with intervals corresponding to midday.**

Table 2. Spatial averaging of pixel response in the AVHRR pixels. Values indicate the average brightness temperature differences (absolute values) of the 25 individual NOAA responses from the colocated GMS pixel value and their standard deviations. Values are presented for both infrared channels (IRC-4 and IRC-5) corresponding to 10.3-11.3 µm and 11.5-12.5 µm respectively.

		IRC-4		IRC-5	
		3x3 – Single	5x5 – Single	3x3 – Single	5x5 – Single
Period 1	Mean Difference ($\overline{T}$)	0.160	0.279	0.144	0.224
	Std. Deviation (σ)	0.117	0.464	0.122	0.396
Period 2	Mean Difference ($\overline{T}$)	0.215	0.188	0.203	0.188
	Std. Deviation (σ)	0.392	0.186	0.316	0.177

The differences observed between the two infrared channels on the AVHRR and their corresponding channels on the GMS may be related to differences in the overlap of the spectral response curves, or filter functions. Examination of these filters indicates that there is greater overlap in the infrared regions being sensed for the GMS response than those for the AVHRR. Thus the GMS channels are more strongly correlated to each other than the AVHRR channels. These functions are reproduced in Appendix 2.
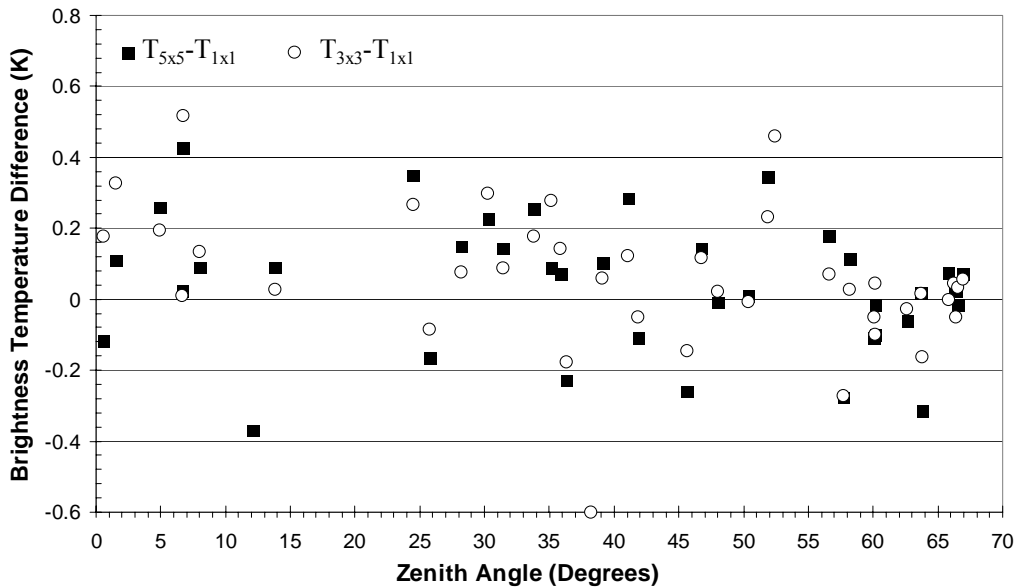
Figure 3. Observed differences between the 3x3 and 5x5 NOOA brightness temperature averages and the central NOAA pixel for changes in zenith angle. Data from Infrared Channel 2 (11.5-12.5 µm) was used for this diagram.

The following points provide a further analysis of the individual channel responses for each of the studied periods, illustrated in Figure 2.

i. The diurnal peak for the GMS platform matches up reasonably well with the NOAA values. The daily peak is the major area of discrepancy between the four individual GMS responses, with the remaining GMS observations agreeing quite

well. The ascending side of the diurnal curve is extremely well matched for all the GMS signatures.

ii. An apparent dampening of the diurnal amplitude, can be observed between the infrared channels for both periods. This is generally constrained around the diurnal peak, with the night time values of both the GMS and NOAA observations not as greatly affected by the apparent compression. Interestingly, this feature is more marked in the NOAA-AVHRR although it is still evident in the GMS brightness values. Data values can be examined in Table 3.

iii. The effect of this flattening is to increase the difference between peak GMS and NOAA values. There is a consistent negative bias within the NOAA values at the peaks, such that they underestimate the GMS response by up to 2.5K in some places (18 March, 3.18 p.m.).

iv. Spatial variation in the surface temperatures of adjacent GMS pixels is greatest at night, at the time when least surface temperature difference would be expected. This is most likely due to cloud cover rather than contamination by water as the patterns throughout the day match well. There is also a small amount of variation at the daytime peak.

Additional analysis is provided in Table 3 which examines brightness temperature differences at the diurnal peaks between the platforms and Table 4 which presents root mean square errors (RMS) and correlation coefficients (r^2) for the 41 coincident NOAA and GMS responses.

Table 3. Differences in the peak brightness temperatures across the NOAA and GMS platforms, as shown in Figure 2. Abbreviations for the infrared channels (IRC) correspond to the following wavelengths: IRC-1 (10.5-11.5 μm), IRC-2 (11.5-12.5 μm), IRC-4 (10.3-11.3 μm) and IRC-5 (11.5-12.5 μm). Units are K.

Colocated GMS-VISSR			NOAA-AVHRR Responses					
			1x1			5x5		
IRC-1	IRC-2	Diff	IRC-4	IRC-4	Diff	IRC-4	IRC-5	Diff
290.63	289.55	1.07	293.55	291.40	2.15	294.10	291.68	2.41
297.70	296.64	1.05	295.80	293.25	2.55	296.11	293.59	2.51
302.86	301.74	1.12	301.45	298.80	2.65	301.30	298.69	2.61
293.02	291.78	1.25	294.05	292.05	2.00	293.58	291.68	1.90
291.52	290.94	0.58	295.05	292.90	2.15	295.14	292.92	2.21
293.33	292.75	0.59	295.65	293.90	1.75	296.16	294.25	1.91
292.61	291.70	0.91	295.40	292.60	2.80	295.42	292.70	2.72
297.72	296.23	1.49	298.00	295.65	2.35	298.08	295.66	2.42
	Mean	1.01		Mean	2.30		Mean	2.34

Table 4. RMS and r² estimates for coincident NOAA 5x5 and GMS responses. Abbreviations for the infrared channels correspond to the following wavelengths: IRC-A (10.3-11.5 μm) and IRC-B (11.5-12.5 μm). Day time overpasses (07:00-19:00) and night time overpasses (19:00-07:00) are also shown.

	All Records		Day Time		Night Time	
	IRC-A	IRC-B	IRC-A	IRC-B	IRC-A	IRC-B
RMS (K)	1.53	1.39	1.79	1.71	1.20	0.95
r²	0.90	0.88	0.83	0.78	0.73	0.74
Sample	41		21		20	

3. Brightness Temperature Variations between the GMS-VISSR and NOAA-AVHRR Satellites.

The variation of brightness temperature estimates between the two platforms is a significant factor in ultimately determining accurate LST patterns from these sensors. Generating a refined temporal sequence from both platforms or even applying algorithms from one sensor to the other demands that a close correlation between the two can be preserved throughout the diurnal response. The following section provides an examination of the brightness temperature differences across platforms and offers some possible explanations for the emerging patterns across the two periods. Some of the issues that will be discussed include the effects of spatial averaging on the derived brightness values, the diurnal variation in brightness temperatures and the influence of the sun-target-sensor geometry, in particular the satellite zenith angle on brightness temperatures.

Spatial Aggregation Issues

Heterogeneity is a feature of all natural surfaces. Techniques to resolve the effects of variation in surface properties continue to complicate and confound the modeling of land surface responses. There are difficulties in aggregating individual responses to arealy averaged values as many of these land surface responses are non-linear in nature. The estimation of LST provides an ideal example, with the non-linear nature being a product of the Planck function. For the estimation of land surface parameters using remote sensing, issues of spatial heterogeneity and resolution are particularly pertinent. LST can vary substantially throughout all scales, from just a few meters to several kilometres. It would be expected that as the spatial resolution becomes more coarse, the degree of difference would be reduced as spatial averaging of remotely sensed variables dampens local scale fluctuations such as those resulting from soil moisture variation, shading and vegetation cover. As such, it would be expected that the degree of variation within the NOAA pixels would be greater than that for the GMS over a similar area.

The following discussion focuses on the variation within a small sub-section of the study area, covering approximately 25 km². The region comprises 25 NOAA-AVHRR pixels that have been colocated with a single GMS-VISSR pixel. In order to examine

the spatial variability in brightness temperature within this area 1x1, 3x3 and 5x5 spatial averages were extracted and examined for spatial patterns throughout the time series under investigation.

Spatial Averaging

The averaging of information is an integral component of remote sensing. Remote measures of the land surface detect an arealy weighted average response at the pixel scale. The fractional weighting of the various discrete land surface elements that compose a single pixel response is uncertain. A number of studies have investigated the effects of surface heterogeneity on a variety of land surface parameters including the LST (Chehbouni *et al.*, 1995; Njoku *et al.*, 1996) and it is generally recognised that the radiation sensed at the satellite level is a non-linear coupling of the underlying, individual surface components.

The degree of uncertainty in the derived brightness temperature will be related to the relative variability in the sensed surface. For example, a relatively uniform surface will produce a more representative brightness temperature than one from an area exhibiting a high degree of variability. The aggregation of the single (central) NOAA pixel to the 3x3 and 5x5 averages was an attempt to examine the effects of linear averaging on the brightness temperature and to characterise the role that small scale heterogeneities within the pixel response have on averaged values. This also provides an opportunity to relate the derived value to the single GMS pixel, by scaling to an equal areal representation. Generally, averaging of the radiances, then conversion to a brightness temperature would be the preferred process. The more heterogeneous a surface is, the greater is the need to use radiances due to the non-linearity of the Planck function. The averaging of the brightness temperatures instead of radiances was deemed acceptable due to the perceived level of heterogeneity in the landscape, as discussed previously in Section 2, and illustrated in Figure 1.

Table 5 presents statistics relating the 3x3 and 5x5 average brightness temperatures to the single pixel response for both channels and periods. Values given are the absolute differences between the spatial averages and the subsequent statistical measures are calculated from these absolute values. As can be seen there is a slight increase in the average brightness temperature during Period 1, while there is a small decrease in Period 2 as the spatial area is increased. As expected, the statistics are similar across the two infrared channels.

Table 5. Spatial averaging of pixel response in the AVHRR pixels. Values indicated are the average temperature differences (absolute values) of the 25 individual NOAA responses from the colocated GMS pixel value. Values are presented for both infrared channels (IRC-4 and IRC-5) corresponding to 10.3-11.3 μm and 11.5-12.5 μm respectively.

		IRC-4		IRC-5	
		3x3 – Single	*5x5 – Single*	*3x3 – Single*	*5x5 – Single*
Period 1	*Average Difference ($\overline{T}$)*	0.160	0.279	0.144	0.224
	Standard Deviation (σ)	0.117	0.464	0.122	0.396
Period 2	*Average Difference ($\overline{T}$)*	0.215	0.188	0.203	0.188
	Standard Deviation(σ)	0.392	0.186	0.316	0.177

Figure 4 samples early morning, sunrise, midday and sunset NOAA overpasses, extracted across an 11x11 pixel area. These images illustrate the typical level of variability in brightness temperatures across the study area at different times throughout the day. Images have been projected onto a uniform grid so, depending on the zenith angle, areas may not be strictly equivalent. The central pixel in each image corresponds to the value used for the single NOAA response, with subsequent 3x3 and 5x5 values averaged in windows around this pixel. Some additional information and simple statistics are presented with each image. A colour bar has been associated with each image, corresponding to the range of responses within individual overpasses.

As can be seen, the greatest variation occurs during the middle of the day, with an associated standard deviation in excess of 1K. Generally though, 3x3 and 5x5 averages correspond well to the image average, indicating that while inter-pixel variability exists, its effect is not particularly large. The variation of pixel brightness values throughout the day is a function of a number of contributing factors including the energy balance, differential heating of the surface, moisture influences and other local meteorological influences. This variation is explored further in the following section.

Variation Throughout the Diurnal Cycle.

In a non-homogenous landscape, the degree of variability observed within the spatially averaged pixels would be expected to vary during the course of the diurnal cycle. Intuitively, the variability in brightness temperature during the night should be less than that during the day. This is due primarily to the absence of direct solar radiation and the influence of differential heating of the land surface. Also, the soil moisture and exchanges of latent and sensible heat fluxes during the day would affect the surface response. One of the features of the temporal patterns observed in Figure 2 and also in Figure 4, was the tendency for the difference in brightness temperatures to be most marked during the hottest part of the day, excluding the effects of intermittent cloud cover. This is to be expected, as there is a high degree of interacting energy dynamics – surface heating, horizontal advection, and vegetation influences.

	Satellite Number.	NOAA-14_11501
	Time of Overpass.	01:39:42
	Zenith Angle. (Deg)	7.932
	Min Temp. (K)	285.20
	Max Temp. (K)	290.45
	Mean Temp. (K)	287.10
	Standard Deviation.	0.9495
	Variance.	0.9015
	3x3 Average (K)	287.095
	5x5 Average (K)	286.986

	Satellite Number.	NOAA-12_30323
	Time of Overpass.	06:22:02
	Zenith Angle. (Deg)	35.832
	Min Temp. (K)	288.10
	Max Temp. (K)	292.00
	Mean Temp. (K)	289.33
	Standard Deviation.	0.6283
	Variance.	0.3947
	3x3 Average (K)	289.261
	5x5 Average (K)	289.186

	Satellite Number.	NOAA-14_11550
	Time of Overpass.	13:28:10
	Zenith Angle. (Deg)	58.954
	Min Temp. (K)	292.60
	Max Temp. (K)	298.20
	Mean Temp. (K)	295.405
	Standard Deviation.	1.4185
	Variance.	2.0122
	3x3 Average (K)	295.928
	5x5 Average (K)	295.712

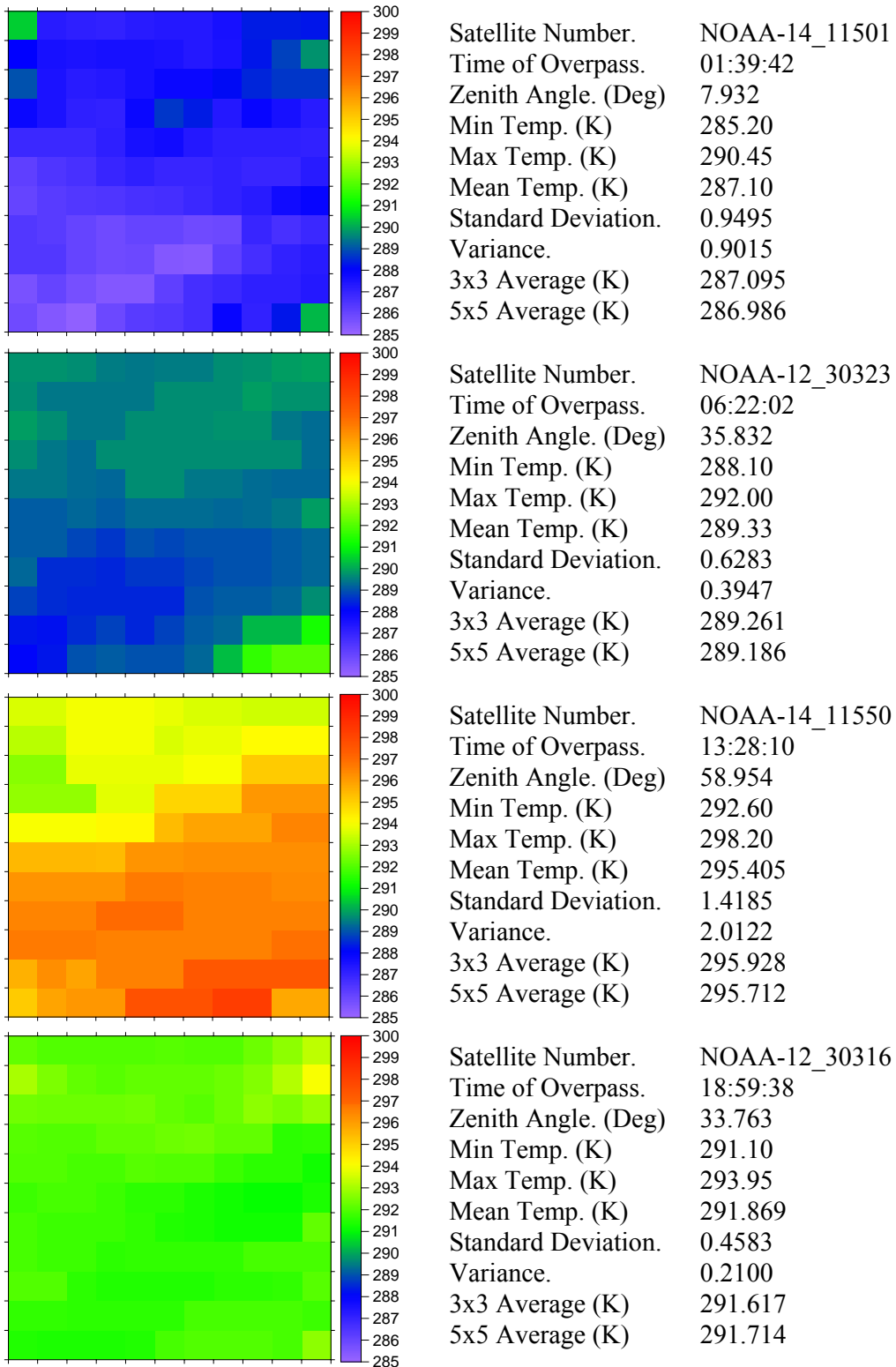|	Satellite Number.	NOAA-12_30316
	Time of Overpass.	18:59:38
	Zenith Angle. (Deg)	33.763
	Min Temp. (K)	291.10
	Max Temp. (K)	293.95
	Mean Temp. (K)	291.869
	Standard Deviation.	0.4583
	Variance.	0.2100
	3x3 Average (K)	291.617
	5x5 Average (K)	291.714

Figure 4. Variation in the brightness temperature for Channel 4 of the AVHRR (10.5-11.5 μm) across an 11x11 area with (top to bottom) early morning, sunrise, early afternoon and sunset overpasses. Images are projected onto an equal sized grid rather than the actual pixel size of the individual image for clarity.

Effect on the Spatial Averages.

To analyse this diurnal variation further, differences between the NOAA 3x3 and 5x5 spatial averages from their central pixel were plotted against the time of overpass (see Figure 5). Examination of this figure confirms the lack of variation observed between the spatial temperature averages throughout the course of the day. The majority of values are within ±0.5K of the central pixel throughout the diurnal trend, with the least amount of variation occurring in the early morning overpass (1-3 a.m.). There is no discernible pattern evident between the 3x3 and 5x5 averages throughout the day. An analysis of the difference between the averages was undertaken to examine whether any insight into heterogeneities at the surface could be gained from knowledge of any variation throughout the diurnal trend. The differences between the 3x3 and 5x5 averages were plotted for both infrared channels against the time of overpass, and are shown in Figure 6.

A slight pattern emerges on examination of the spatial differences throughout the course of the day. Most notable are the more positive differences occurring around the diurnal peak (1-3 p.m.), indicating that there is a degree of spatial variation in brightness temperatures during this period. Also, a negative trend is observed in the sunrise period (5-7 a.m.), while the other periods are fairly equally distributed. The temperature differences for all these periods however, is not particularly large with most lying between ±0.25K, indicating a relatively homogeneous surface.
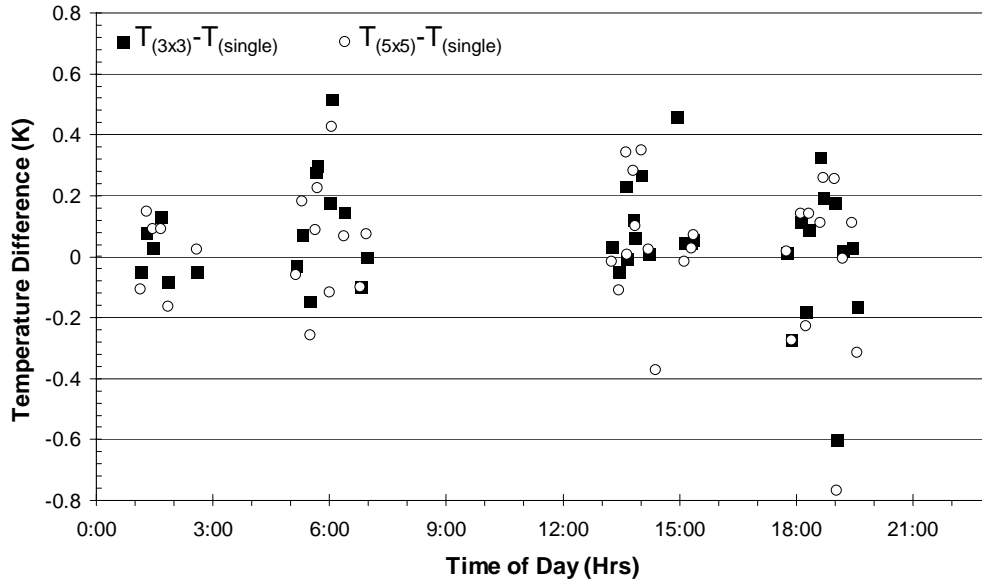

Figure 5. Variation of NOAA brightness temperature in IR-Channel 5 (11.5-12.5 μm) of the AVHRR throughout the day. The values indicated are the temperature differences between the 3x3 and 5x5 spatial averages and the single pixel response. Values are taken across both periods and consist of 40 responses.
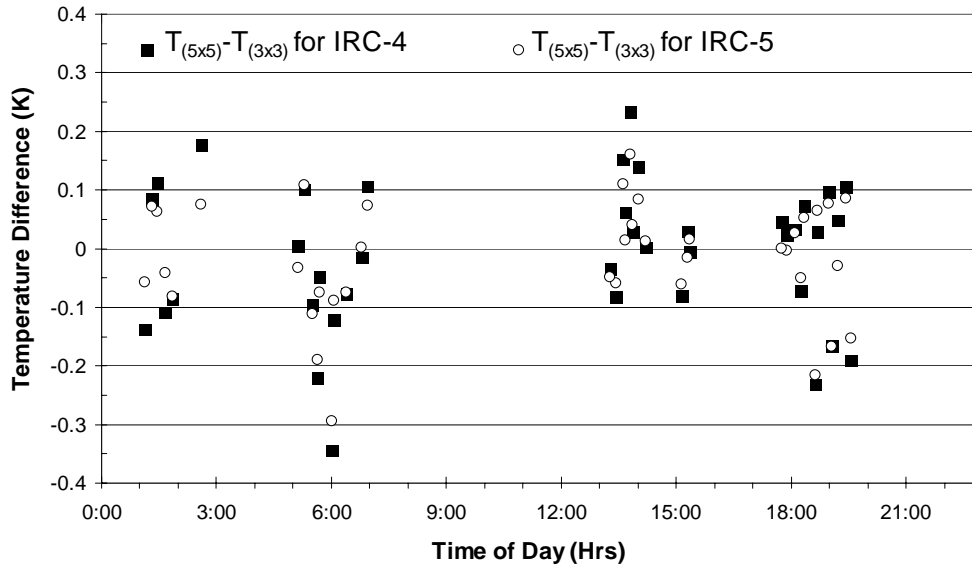
Figure 6. Difference between the 3x3 and 5x5 spatially averaged brightness temperatures extracted from the NOAA-AVHRR. The values shown represent both infrared channels (IRC-4 10.3-11.3 μm and IRC-5 11.5-12.5 μm) plotted against the time of overpass in local time.

Spatial Variation Across Infrared Channels.

One of the features observed in Figure 2 was the difference between the two infrared channels, particularly during the afternoon peak of the diurnal cycle. An interesting feature emerges from closer examination of the differences between the infrared channels on both the NOAA and GMS satellites. These were plotted against the time of overpass (local time) and are illustrated in Figure 7. Only GMS pixels coincident with the NOAA values were included. As can be seen, the GMS differences are significantly less affected by disparities between the infrared channels than the corresponding NOAA values. The average absolute difference for the coincident GMS is 0.52K (average for all records is 0.57K) compared to 1.29K for the AVHRR records.

The most interesting feature of Figure 7 is the variation throughout the day, especially during the afternoon overpass. This period is significantly affected by temperature differences between the channels. Importantly, this indicates that the variation is not systematic and cannot be attributed to the filter functions alone. While the GMS values may be more highly correlated with the filter functions than the NOAA channels, similar diurnal fluctuations can still be observed.
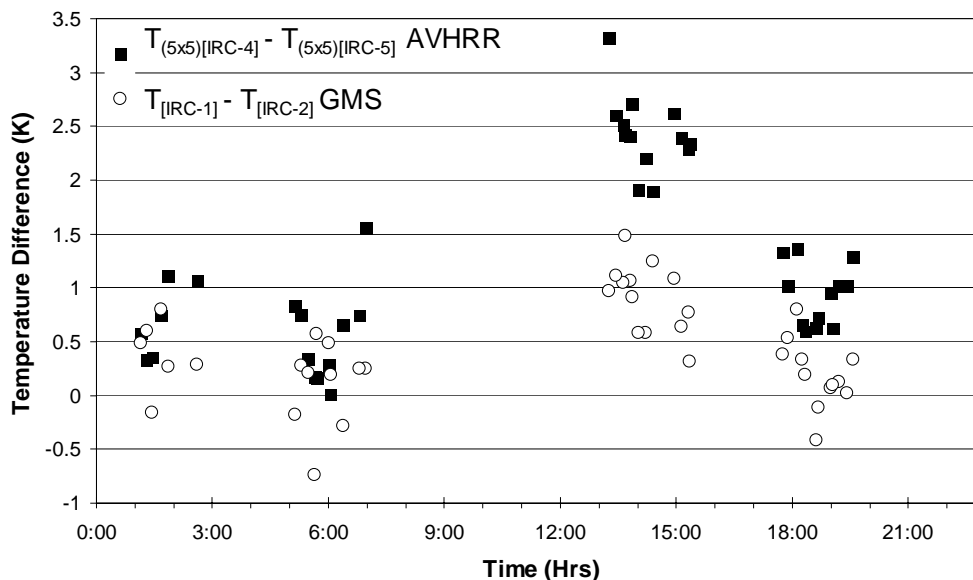
Figure 7. Brightness temperature differences between infrared channels on board the GMS and NOAA satellites (IRC-4 – IRC-5). Values are shown for both periods and record the difference between the 10.3-11.3 μm and 11.5-12.5 μm spectral regions.

The variability of brightness temperatures throughout the day has some important implications for the accurate prediction of LST. The use of different coefficients for night and day time values in the split window equation is generally recognised. Applying this to GMS records however, may produce uncertain results owing to the smaller diurnal differences in inter-channel variations, in comparison to the NOAA values. This discrepancy may prove important in the production of a temperature record combining the NOAA and GMS data streams. The differences observed in the diurnal peak may need to be accounted for.

Angular Effects in NOAA and GMS Satellites

Unlike the GMS platform which has a fixed viewing angle of approximately 50°, the polar orbiting NOAA-AVHRR has a variable scan angle to ±55°, equivalent to a zenith angle of ±68° relative to the earth's surface (Cracknell, 1997). This variable viewing (or zenith) angle causes a variation in both the amount of atmosphere through which sensed radiation from the surface must travel, and in the geometry of the target at the surface, as shown in Figure 8. The atmospheric transmittance is an important variable in determining LST. Prata *et al.* (1995), described this value as being directly dependant on the length of the path travelled, and thus proportional to the secant of the zenith angle. The authors also showed that the range of variation in the atmospheric transmittance is greater for moist atmospheres, illustrating the dependence of the absorption on the atmospheric water vapour content.
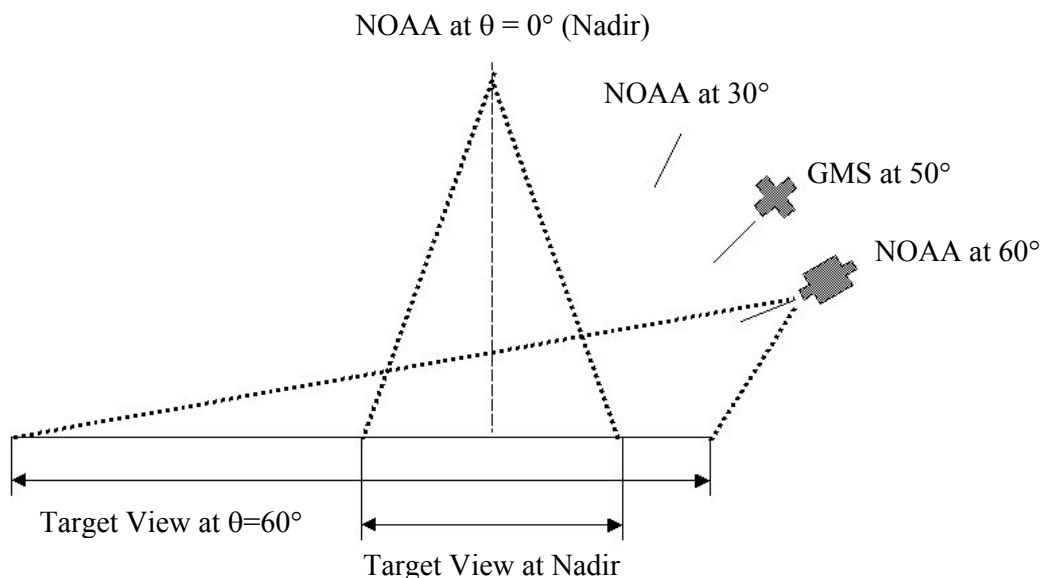
NOAA at θ = 0° (Nadir)

NOAA at 30°

GMS at 50°

NOAA at 60°

Target View at θ=60°

Target View at Nadir

Figure 8. Depiction of the variable viewing geometry associated with the GMS and NOAA-AVHRR satellites. The illustration of the target area is not representative of that seen by the satellites, although pixel distortion occurs at low zenith angles.

One of the aims of this investigation was to examine the effects of variable viewing geometry for NOAA-AVHRR and GMS satellites. The degree to which brightness temperatures are affected by angular variations is a significant consideration in the accurate estimation of LST. The study of angular effects within remotely sensed images has been an active area of research for many years with many studies focussing on bi-directional reflectance distribution functions (BRDF) (Kennedy *et al.*, 1997; O'Brien *et al.*, 1998). Examination of such an effect on surface temperatures has generally been limited to laboratory investigation (Labed and Stoll, 1991; Lagouarde *et al.*, 1995) rather than actual remote sensing platforms. Few studies have focussed on comparisons between the brightness temperatures between the GMS and NOAA platforms.

Desormeaux *et al.* (1992) examined the normalisation of the radiometric calibration of image radiances for a suite of geostationary satellites as part of the International Satellite and Cloud Climatology Project (ISCCP). The study focused on coincident NOAA-AVHRR images with the same viewing geometry as the geostationary platforms and aimed to apply the NOAA absolute calibrations to the radiometers onboard the geostationary satellites. While this investigation also relies on concurrent images, we are primarily interested in the effects of the varying viewing geometry of the AVHRR.

Zenith Angle Relation to Brightness Temperature Difference

In order to examine the effects of varying zenith angles, the difference in brightness temperature between the GMS and NOAA platforms was plotted against the zenith angle. The satellite zenith look angle for the NOAA-AVHRR varies ±68° from nadir, while the GMS has a constant angle for the study area of approximately 50°. The variation in NOAA zenith values allows a direct comparison to be made with the

18

constant viewing angle brightness estimates of the GMS. It is expected that the differences between the two platforms would be at a minimum when they are at the same zenith angles, as it is at this point that they are subject to the same land surface geometry effects and the same atmospheric path length. The zenith angle is often included in LST algorithms due to its correlation to path length and hence atmospheric transmission. It is expected that an understanding may be gained about the relationship between the zenith angle and brightness temperature differences.

Figure 9 illustrates the brightness temperature differences observed between the GMS and NOAA satellites plotted against zenith angle for values in the infrared region 11.5-12.5 µm. The differences were discriminated for night and day occurrences. This was done to delineate any disparity between the responses over the diurnal period. As can be seen, the day time values show significant variation in brightness temperature with increasing zenith angles compared to the night time values, with the range spreading from –2 to 3K compared to ±1K at night. The same response is observed within the infrared region 10.5-11.5 µm, although values are vertically shifted down.

There appears to be no consistent equality between the two platforms for the same viewing angle. This may be due to a number of factors including different satellite calibrations and the higher radiometric resolution of the NOAA satellite when compared to the GMS (10bit to 8bit). There is however, a clear trend to more positive temperature differences as the zenith angle increases. As the day time NOAA satellite passes below the GMS (50°) towards the horizon (90°), the temperature differences are exclusively positive.
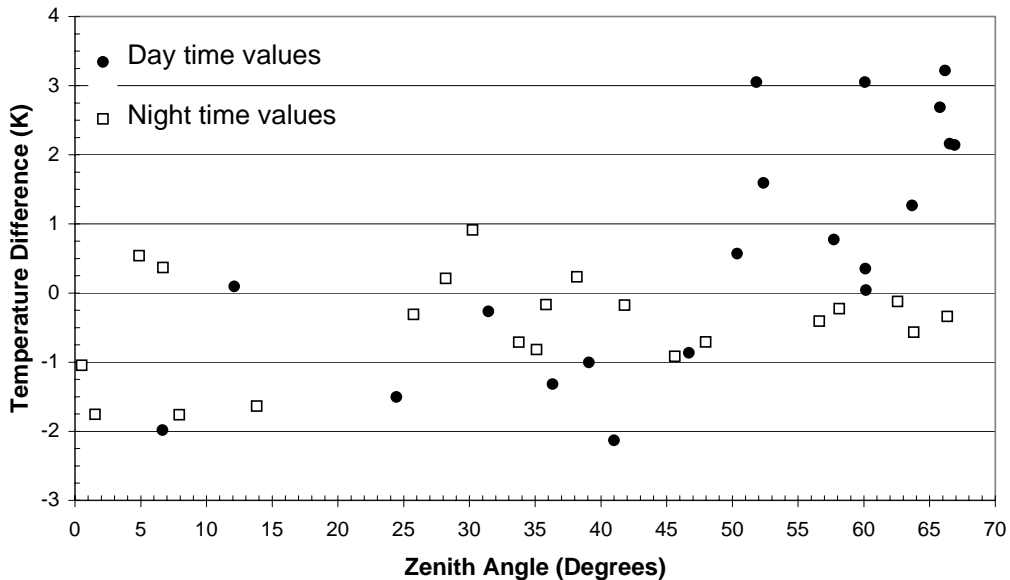

Figure 9. Brightness temperature differences between the GMS and NOAA satellites against satellite look zenith angle. The difference in temperature is the GMS minus the NOAA 5x5 brightness value for infrared values in the 11.5-12.5 µm range. The zenith angle is extracted from the NOAA records. GMS and NOAA satellites have same viewing angles at approximately 50°.

19

The tendency towards increasing temperature differences with zenith angles could be related to either variation in atmospheric absorption, owing to the increased path length from the target to the sensor, or possibly to angular variations in emissivity. While we are unable to fully account for the atmospheric influences on the temperature differences due to the absence of atmospheric soundings, some preliminary investigations into variation of emissivity with viewing angle can be attempted.

Zenith Angle Effects on Emissivity

Variation in the land surface emissivity may significantly alter the accurate retrieval of LST from remote sensors. Few measurements of the angular variation of emissivity over the land surface have been conducted. Barton and Takashima (1986), reported on measurements over a bare surface in the spectral region 10-12 μm, and found variations in emissivity from 0.97 at 30° decreasing to 0.95 at 60°. Spectral variation in emissivity ($\varepsilon_{\lambda,\theta}$), can have a significant effect on the estimation of LST. Becker (1987), proposed a method for determining the error generated in the split-window derived surface temperature (δT), for differences in the ground emissivity between two AVHRR channels. This expression has the form:

$$\delta T \cong 50\frac{(1-\varepsilon)}{\varepsilon} - 300\frac{\Delta\varepsilon}{\varepsilon} \qquad \textbf{Eq. 2}$$

where: ε = the average emissivity
           $\Delta\varepsilon$ = emissivity difference between infrared channels.

Assuming an average ground emissivity of 0.97 and an emissivity difference $\Delta\varepsilon$ of 0.002, the resulting δT estimate approaches 1K. Schmugge *et al.* (1991), using thermal infrared multi-spectral scanner (TIMS) data, reported emissivity variations of around 0.1 for bare soils between infrared channels 3 and 4 (0.9-10 μm), although the effects were limited for water and vegetation. The number of studies examining the angular effects in emissivity are limited and actual measurements are very rare.

As can be seen in Figure 9, there is a sharp increase in the temperature difference between the GMS (fixed zenith angle) and the NOAA satellite (variable zenith angle) around the 45-50° point. This is an interesting feature that was also observed by Lagouarde *et al.* (1995). They reported on an experimental study of angular effects for a variety of surface types and conditions and found that the difference between oblique and nadir observations for a smooth bare soil were below their significance level of 0.5K, except when the viewing angles exceeded 45°. This was attributed to angular variations in emissivity as it was reasoned that the smooth soil should remove directional effects. Labed and Stoll (1991), measured angular variations in emissivity over four different bare agricultural soils. Results from their study showed similar patterns across the soil types for the measured mean emissivity in the 10.6-12 μm portion of the electro-magnetic spectrum. The emissivity was observed to remain fairly constant up to 30°, beyond which it progressively dropped.

As observed in Figure 9, daytime brightness temperature values are significantly affected by variations in the zenith angle with the difference between the GMS and NOAA brightness values increasing with the zenith angle. In order to characterise this

variability, it was reasoned that discrepancies are the result of surface rather than atmospheric influences. These surface influences are a function of the variation in emissivity as the zenith angle increases. This assumption is supported by the smaller degree of variability in the night time values, when atmospheric effects would be most easily distinguished. Prata (1994a) examined the variations of viewing geometry on the measurements of the land surface temperature and proposed the following parameterisation for the angular effect;

$$\varepsilon_s(\theta) = \varepsilon_s(0)\left[\frac{1-\exp\left\{-d_0\cos\left(\theta/d_1\right)\right\}}{1-\exp\left\{-d_0\right\}}\right]$$

Eq. 3

where: θ = viewing angle
$\varepsilon_s(\theta)$ = the directional emissivity at θ
$\varepsilon_s(0)$, d_0 and d_1 are adjustable constants.

To correct the brightness values for these surface effects, the emissivity parameterisation of Prata (1994a) was incorporated into the calculation of a surface corrected brightness value. The adjustable parameters $e_s(0)$, d_0 and d_1 were assigned values of 0.97, 4.40 and 1.35 respectively so as to best fit the observed data and the downward atmospheric irradiance (L$\downarrow$) assigned a value of 20 W.m^{-2}. The adjusted brightness values were determined through a number of steps outlined below.

The radiance emitted by a blackbody is a function of the wavelength and temperature, and is described by the Planck function. This can be expressed in either of the following forms;

$$B_\lambda[T] = \frac{2\pi hc^2}{\lambda^5[\exp(hc/\lambda kT)-1]} = \frac{C_1}{\lambda^5[\exp(C_2/\lambda T)-1]}$$

Eq. 4

where: $B_\lambda[T]$ = Planck function at satellite (W.sr^{-1}.m^{-2})
h = Planck constant (6.626 x 10^{-34} J.s)
c = speed of light (2.998 x 10^8 m.s^{-1})
λ = wavelength (μm)
k = Boltzmann constant (1.38 x 10^{-23} J.deg^{-1})
T = temperature of the source (K)
C_1 = $2\pi hc^2$ = 3.741775 x 10^{-16} W.m^2
C_2 = hc/k = 1.48769 x 10^{-2} m.K

The surface emittance can be related to the radiative surface temperature through the expression;

$$R_{\lambda,\theta} = \varepsilon_{s(\lambda,\theta)}B_\lambda[T_s] + \left[1-\varepsilon_{s(\lambda,\theta)}\right]\Gamma L\downarrow$$

Eq. 5

where: $R_{\lambda,\theta}$ = emittance from the surface (W.sr^{-1}.m^{-2})
$B_\lambda[T_s]$ = Planck function at the surface (W.sr^{-1}.m^{-2})
T_s = brightness temperature at surface level (K)

ε_s = surface emissivity
Γ = atmospheric and channel dependant parameter
$L\downarrow$ = downward atmospheric irradiance (W.m^{-2}).

An estimate of $B_\lambda[T_s]$ was determined using the daytime GMS and NOAA brightness temperatures, which were then substituted into Eq. 4. The directional emissivity term $e_{s(\lambda,\theta)}$, which only varies for the NOAA-AVHRR as the GMS has a fixed zenith angle of 50°, is derived using Eq. 2.

The corrected brightness temperature (T_c) is then calculated by inverting Eq. 3 and re-arranging it in the following form;

$$T_C = \frac{C_2}{\lambda \ln\left(\frac{C_1}{\lambda^5 B_\lambda[T]} + 1\right)} \qquad \textbf{Eq. 6}$$

Corrected temperatures were calculated for both infrared channels on board the GMS and NOAA satellites. The difference between the two sensors was taken for each channel and then compared to the uncorrected values. Both infrared channels displayed similar features with a marked increase in differences above 50°. Figure 10 illustrates the results for correction of the directional emissivity in the infrared region 11.5-12.5 μm.
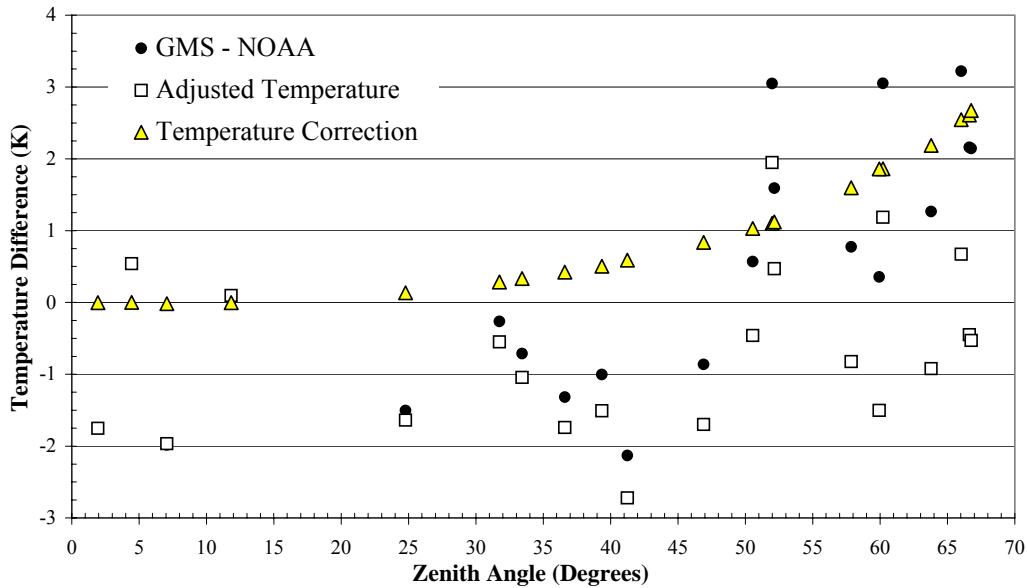

Figure 10. Surface corrections for emissivity variations with zenith angle as described by Eq. 2. Values shown are the corrected and uncorrected temperature differences (GMS-NOAA) for the 11.5-12.5 μm infrared channel.

As can be seen, the corrections in brightness temperatures significantly reduce the positive differences occurring in the uncorrected values for zenith angles greater than 50°. Over double the number of original values are now constrained in the ±1K

temperature bound for θ>50°. Although some corrected values have there differences increased most of these are for brightness difference at zenith angles less than 50°. Improvements in RMS errors from 1.71K to 1.31K resulted from application of this simple correction routine. There was also a corresponding increase in the r^2 correlation coefficient from 0.79 to 0.90.

This technique shows the potential improvements that can be achieved through the use of an angular dependent emissivity term in calculations of surface temperatures. Although only a simple analysis was undertaken more detailed fitting of the surface correction factors in Eq. 3 should provide increased accuracy. An investigation comparing a larger number of coincident NOAA-AVHRR overpasses should be undertaken to further assess the effect of increasing zenith angles on predictions of surface temperatures and their relation to GMS estimates.

4.   Concluding Remarks and Future Work

An examination of the differences between the GMS-VISSR and NOAA-AVHRR satellites was undertaken with the aim of reproducing a temporal sequence of land surface temperatures. Brightness values in both infrared channels were compared between platforms for a period of approximately ten days. Issues of geographic correction, spatial resolution and heterogeneity at the land surface were encountered and have been discussed. It was shown that a time series of brightness temperatures can be readily extracted, although contamination through cloud coverage provides the greatest hindrance to collecting an uninterrupted record. Use of NOAA values offers a valuable source of information from which to compare land surface predictions, especially when ground based information is not available.

The diurnal cycle of land surface brightness temperature was clearly represented in the GMS sequence. Coincident NOAA values were included to compare values and obtain insight into the variability in surface brightness temperature at different spatial scales. NOAA brightness values generally matched well with their corresponding GMS temperatures, particularly at night time and in the early morning. There is a consistent disparity however between the peak estimates of the GMS and NOAA records however. This difference is also prominent between infrared channels, with the NOAA having at least an additional 1K difference to that measured between the same GMS infrared channels.

Some variability in temperature differences throughout the day was observed between platforms. This variability has implications with regards to the use of surface temperature algorithms across platforms. The use of different split window algorithm coefficients for day and night time values is already recognised. Applying such coefficients to the GMS records however, may produce uncertain results owing to the reduced differences relative to the NOAA values that these inter-channel variations have over the diurnal trend. This discrepancy is also important in the production of a temperature record combining the NOAA and GMS data streams. The temperature differences observed in the diurnal peaks would also need to be accounted for.

The paper also reported on the angular variations evident in the NOAA platform relative to the geostationary GMS satellite. It was observed that as the zenith angle increased towards the horizon (or below the position of the GMS satellite), the differences between the two became more positive. An attempt was made to correct this disparity through the introduction of an emissivity adjustment. The angular variation in emissivity was incorporated through a simple parameterisation and subsequent brightness temperatures corrected to account for this modification. This reduced the positive differences occurring for angular variations at zeniths greater than fifty degrees.

Utilising these additional sources of information within a soil-vegetation-atmosphere-transfer (SVAT) modelling framework is the focus of continuing research (McCabe *et al.*, 2001). Incorporating additional information is an effective technique in reducing model uncertainty and producing enhanced model predictions. The NOAA-AVHRR offers a valuable data source and has the potential to be used in a number of applications in conjunction with the GMS-VISSR. The high temporal resolution of the GMS coupled with the higher spatial resolution of the NOAA may facilitate the production of a refined estimate of land surface temperature.

The utility of remote sensing to provide near real time estimates of the land surface at a variety of spatial and temporal resolutions is evident. The use of remotely sensed information within a modeling framework, be it hydrological, meteorological or oceanographic, demands suitable procedures to utilise these data sources effectively. Combining data streams from both sources may offer a means of producing a refined product for use in a number of applications. One such approach that may provide a means of achieving this is data assimilation. The underlying principle behind data assimilation is that it aims to improve time dependant and spatially distributed estimates by periodically updating them as new data becomes available. Remote sensing provides an ideal source from which to assimilate data into model structures as it provides regular updates of the 'current' condition of the process under investigation.

5. References

Becker, F. and Li, Z. L. (1995). "Surface temperature and emissivity at various scales: definition, measurement and related problems." *Remote Sens. Rev.* **12**: 225-253.

Boutin, J., Etcheto, J., Dandonneau, Y., Bakker, D. C. E., Feely, R. A. and Inoue, H. Y. (1999). "Sea surface temperature assimilation for a three-dimensional baroclinic model of shelf seas." *Tellus Series B - Chem. Phys. Meteorol.* **51**(2): 490-508.

Chehbouni, A., Njoku, E. G., Lhomme, J. P. and Kerr, Y. H. (1995). "Approaches for averaging surface parameters and fluxes over heterogeneous terrain." *J. Climate* **8**(5 Part 2): 1386-1393.

Coll, C. and Casselles, V. (1997). "A split-window algorithm for land surface temperature from Advanced Very high Resolution Radiometer data: validation and algorithm comparison." *J. Geophys. Res.* **102**: 16,697-16,713.

Cracknell, A. P. (1997). The Advanced Very High Resolution Radiometer. London, UK, Taylor and Francis.

Diak, G. R. and Stewart, T. R. (1989). "Assessment of surface turbulent fluxes using geostationary satellite surface skin temperature and a mixed layer planetary boundary layer scheme." *J. Geophs. Res.* **94**: 6357-6373.

Jackson, T. J. (1997). "Soil moisture estimation using special satellite microwave imager satellite data over a grassland region." *Water Resour. Res.* **33**(6): 1475-1484.

Kennedy, R. E., Cohen, W. B. and Takao, G. (1997). "Empirical methods to compensate for a view-angle dependant brightness gradient in AVIRIS imagery." *Remote Sens. Environ.* **62**: 277-291.

Kerr, Y. H., Lagouarde, J. P. and Imbernon, J. (1992). "Accurate land surface temperature retrieval from AVHRR data with use of an improved split window." *Remote Sens. Environ.* **41**: 197-209.

Kneizys, F. X., Shettle, E. P., Abreu, L. W., Chetwynd, J. H., Anderson, G. P., Gallery, W. O., Selby, J. E. and Clough, S. A. (1988). User's Guide to LOWTRAN-7. Hanscom Air Force Base, MA, Air Force Geophys. Lab.

Kustas, W. P. and Humes, K. S. (1996). Sensible heat flux from remotely-sensed data at different resolutions. *Scaling up in Hydrology using Remote Sensing*. J. B. Stewart, E. T. Engman, R. A. Feddes and Y. Kerr, John Wiley & Sons**:** 127-145.

Labed, J. and Stoll, M. P. (1991). "Angular variation of land surface spectral emissivity in the thermal infrared: laboratory investigations on bare soils." *Int. J. Remote Sens.* **12**: 2299-2310.

Lagouarde, J. P., Kerr, Y. H. and Brunet, Y. (1995). "An experimental study of angular effects on surface temperatures for various plant canopies and bare soils." *Agric. For. Meteorol.*(77): 167-190.

McCabe, M. F., Franks, S. W. and Kalma, J. D. (2001). Improved conditioning of SVAT models with observations of infrared surface temperatures. *Soil Vegetation Atmosphere Transfer Schemes and Large Scale Hydrological Models*. A. J. Dolman, A. J. Hall, M. L. Kavvas, T. Oki and J. W. Pomeroy. Wallingford, UK., Int. Assoc. of Hydrol. Sci. (IAHS). **Publ. 270:** pp. 217–224.

McCabe, M. F., Prata, A. J. and Kalma, J. D. (2001). The effects of scale in predictions of land surface temperature from a variety of remote sensing platforms. Proceedings of the International Geoscience and Remote Sensing Symposium (IGARSS), Sydney, Australia.

McMillin, L. M. and Crosby, D. S. (1984). "Theory and validation of the multiple window sea surface temperature technique." *J. Geophys. Res.* **89**: 3655-3661.

McVicar, T. R. and Jupp, D. L. B. (1998). "The current and potential operational uses of remote sensing to aid decisions on drought exceptional circumstances in Australia: a review." *Agricultural Systems* **57**(3): 399-468.

Njoku, E. G., Hook, S. J. and Chehbouni, A., Eds. (1996). Effects of surface heterogeneity on thermal remote sensing of land parameters. Scaling up in Hydrology using Remote Sensing. West Sussex, UK, John Wiley & Sons.

Norman, J. M., Divakarla, M. and Goel, N. S. (1995). "Algorithms for extracting information from remote thermal-IR observations of the Earths surface." *Remote Sens. Environ.* **51**: 151-168.

Norman, J. M., Kustas, W. P., Prueger, J. H. and Diak, G. R. (2000). "Surface flux estimation using radiometric temperature: A dual temperature-difference method to minimize measurement errors." *Water Resour. Res.* **36**(8): 2263-2274.

Nunez, M. and Kalma, J. D. (1996). Satellite mapping of the surface radiation budget. *Advances in Bioclimatology*. G. Stanhill. Berlin, Springer-Verlag**:** 63-124.

O'Brien, D. M., Mitchell, R. M., Edwards, M. and Elsum, C. C. (1998). "Estimation of BDRF from AVHRR short-wave channels: Tests over semiarid Australian sites." *Remote Sens. Environ.* **66**: 71-86.

Prata, A. J. (1993). "Land surface temperature derived from the advanced very high resolution radiometer and the along-track scanning radiometer 1. Theory." *J. Geophys. Res.* **98**(D9): 16,689-16,702.

Prata, A. J. (1994). Infrared measurement of land surface temperature from space and the effects of viewing geometry. Proc. of the 6th Symposium on Physical Measurements and Signatures in Remote Sensing, Val d'Isère.

Prata, A. J. (1994). "Land surface temperature determination from satellites." *Adv. Space Res.* **14**(3): 15-26.

Prata, A. J. and Cechet, R. P. (1999). "An assessment of the accuracy of land surface temperature determination from the GMS-5 VISSR." *Remote Sens. Environ.* **67**(1): 1-14.

Seguin, B., Courault, D. and Guerif, M. (1994). "Surface temperature and evapotranspiration: Application of local scale methods to regional scale using satellite data." *Remote Sens. Environ.* **49**: 287-295.

Appendix A

Table 6. Concurrent NOAA-AVHRR and GMS brightness temperatures. The GMS temperatures correspond to the solid line as shown in

| Date	Time	AVHRR Channel 4			AVHRR Channel 5			Zenith	GMS Temps		Time
(EST)	(EST)	1x1	3x3	5x5	1x1	3x3	5x5	Angle	IRC-1	IRC-2	(EST)
					Period 1						
16/03/97	18:59	291.500	291.617	291.714	290.500	290.678	290.756	33.7629	290.115	290.044	19:00
17/03/97	1:26	288.850	288.983	289.096	288.650	288.678	288.742	13.8197	286.948	287.106	1:42
17/03/97	6:22	289.300	289.261	289.186	288.450	288.594	288.520	35.8316	288.071	288.352	6:32
17/03/97	13:48	293.550	293.861	294.096	291.400	291.522	291.684	41.0018	290.627	289.553	13:32
17/03/97	18:37	290.400	290.678	290.446	289.700	290.028	289.812	1.5221	287.647	288.058	18:32
18/03/97	6:00	288.300	288.417	288.072	287.900	288.078	287.784	0.5154	287.227	286.739	6:00
18/03/97	13:37	295.800	295.956	296.108	293.250	293.483	293.594	51.8177	297.698	296.644	13:32
18/03/97	15:18	294.400	294.389	294.420	292.100	292.144	292.130	66.1766	296.129	295.349	15:15
18/03/97	18:15	292.350	292.311	292.238	291.800	291.622	291.572	36.3173	290.591	290.254	18:32
19/03/97	5:38	288.050	288.383	288.162	287.900	288.178	287.988	35.1040	286.432	287.170	5:32
19/03/97	13:26	301.450	301.383	301.302	298.800	298.750	298.692	60.0833	302.861	301.743	13:32
19/03/97	15:07	301.400	301.311	301.232	298.850	298.894	298.834	60.1182	299.836	299.189	15:02
19/03/97	17:53	293.600	293.322	293.346	292.600	292.328	292.326	57.7175	293.635	293.100	17:32
19/03/97	19:34	292.400	292.211	292.020	291.050	290.889	290.736	63.8016	290.507	290.170	19:33
20/03/97	2:35	287.300	287.067	287.244	286.150	286.100	286.176	66.3536	286.125	285.838	2:25
20/03/97	5:17	286.750	286.883	286.986	286.050	286.122	286.232	56.6065	286.109	285.827	5:32
20/03/97	6:57	288.750	288.683	288.790	287.150	287.150	287.224	65.7920	290.164	289.910	7:00
20/03/97	13:15	293.050	293.100	293.066	289.750	289.783	289.736	66.5341	292.871	291.896	13:32
20/03/97	14:56	290.000	290.444	292.172	287.700	288.161	289.542	52.3700	292.220	291.134	15:02
20/03/97	19:12	291.200	291.322	291.370	290.350	290.372	290.344	47.9720	289.766	289.637	19:33
					Period 2						
23/03/97	14:23	294.050	292.278	293.580	292.050	290.656	291.680	12.1129	293.022	291.775	14:25
23/03/97	18:06	291.100	291.078	291.112	289.600	289.717	289.744	46.6921	289.689	288.881	18:00
24/03/97	1:50	287.400	287.389	287.304	286.350	286.267	286.186	25.7411	286.154	285.878	1:42
24/03/97	5:29	284.450	284.339	284.244	284.150	284.006	283.894	45.6215	283.194	282.978	5:32
24/03/97	14:12	295.050	295.133	295.136	292.900	292.911	292.924	6.6526	291.522	290.940	14:25
24/03/97	17:44	288.100	288.161	288.208	286.850	286.867	286.868	63.6767	288.521	288.135	17:32
24/03/97	19:24	288.100	288.178	288.284	287.150	287.178	287.264	58.1322	287.069	287.039	19:33
25/03/97	1:39	286.950	287.094	286.986	286.150	286.283	286.242	7.9317	285.283	284.480	1:42
25/03/97	5:07	285.800	285.867	285.872	285.100	285.072	285.040	62.5622	284.744	284.917	5:32
25/03/97	6:47	286.250	286.267	286.252	285.600	285.500	285.502	60.1581	285.803	285.546	6:32
25/03/97	14:01	295.650	296.022	296.162	293.900	294.167	294.252	24.4424	293.334	292.748	14:00
25/03/97	19:02	288.450	287.922	287.758	287.900	287.300	287.134	38.1744	287.470	287.368	19:00
26/03/97	13:50	295.400	295.389	295.418	292.600	292.661	292.702	39.0951	292.612	291.698	13:32
26/03/97	18:40	288.550	288.661	288.690	287.700	287.894	287.960	4.8761	288.396	288.499	18:32
27/03/97	1:18	286.950	287.000	287.086	286.600	286.678	286.750	28.1830	287.564	286.961	1:42
27/03/97	6:02	285.450	286.017	285.896	285.450	285.967	285.878	6.6826	286.438	286.245	6:00
27/03/97	13:39	298.000	298.022	298.084	295.650	295.644	295.660	50.3625	297.718	296.229	13:32
27/03/97	15:20	294.800	294.722	294.718	292.300	292.356	292.372	66.9107	294.835	294.516	15:32
27/03/97	18:19	291.600	291.667	291.740	291.000	291.089	291.142	31.4335	291.077	290.877	18:32
28/03/97	1:07	289.750	289.706	289.568	289.100	289.050	288.994	41.7910	289.307	288.817	1:42
28/03/97	5:41	286.550	286.844	286.796	286.400	286.700	286.626	30.2465	288.112	287.540	5:32
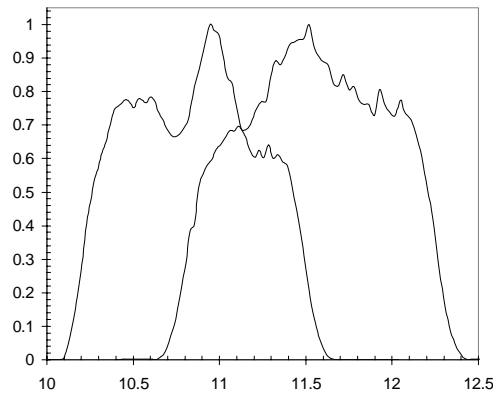
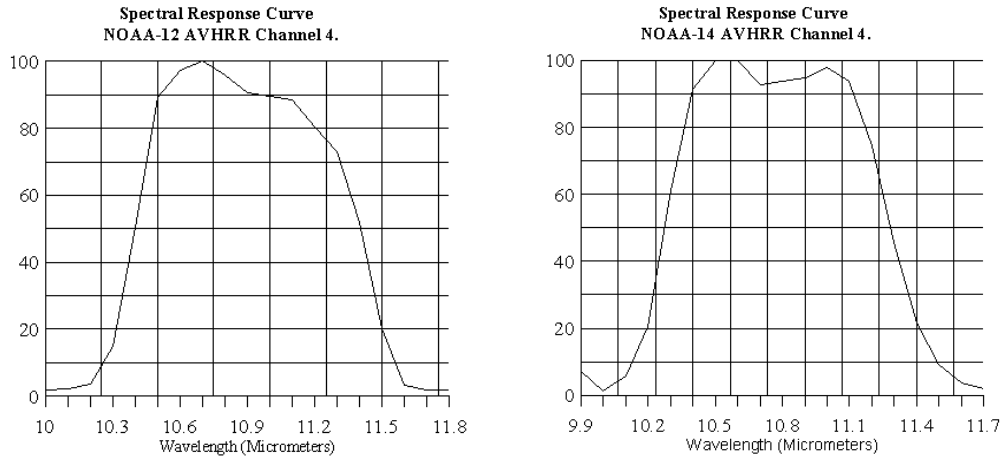**Figure 11. GMS-5 filter function for IRC-1 (left) and IRC-2 (right).**

Figure 12. AVHRR filter functions for channel 4 on-board NOAA-12 (left) and NOAA-14 (right).
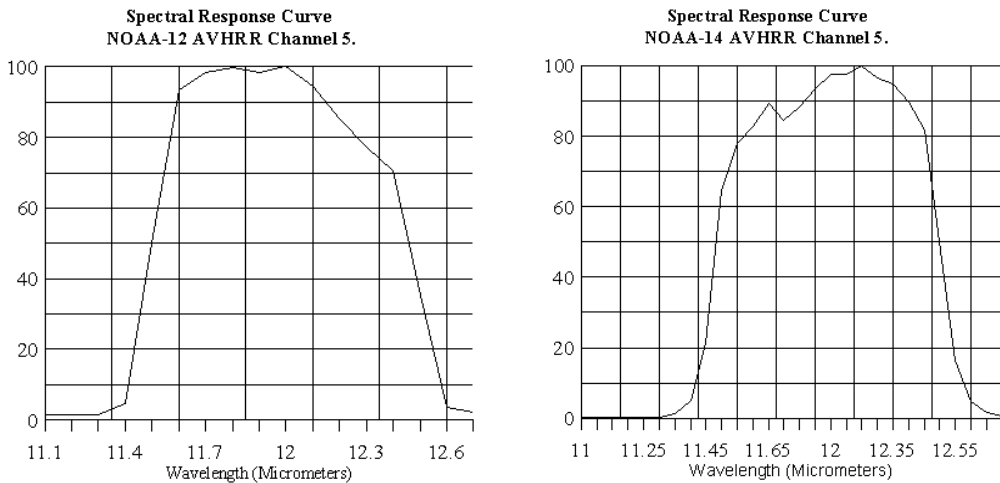

Figure 13. AVHRR filter functions channel 5 on-board NOAA-12 (left) and NOAA-14 (right).